Dynamics of Nonlinear Cross-Equatorial Flow. Part II: The Tropically Enhanced Instability of the Western Boundary Current

CHRISTOPHER A. EDWARDS

Massachusetts Institute of Technology–Woods Hole Oceanographic Institution Joint Program, Cambridge, Massachusetts

JOSEPH PEDLOSKY

Woods Hole Oceanographic Institution, Woods Hole, Massachusetts

(Manuscript received 1 May 1997, in final form 30 January 1998)

ABSTRACT

A linear stability analysis of the shallow-water system in the tropical ocean examines the stability of the western boundary current and its latitudinal dependence. Despite a highly idealized formulation that assumes a purely meridional basic state and makes a local f-plane approximation, the stability analysis successfully predicts a length scale of the disturbance, a latitude for its origin, and a critical Reynolds number that agree well with accompanying numerical results. Realistic western boundary current profiles undergo a horizontal shear instability that is partially stabilized by viscosity. Calculations of the growth rate at several latitudes indicate that the instability is enhanced in the Tropics where the internal deformation radius is a maximum.

1. Introduction

In a companion paper, Edwards and Pedlosky (1998) numerically investigated the potential vorticity transformation of fluid crossing the equator for varying degrees of nonlinearity. A β-plane, shallow-water model confined within a rectangular basin straddling the equator was forced by the injection of a constant mass flux through the northwestern corner. Dissipation was parameterized as momentum diffusion. The Reynolds number was defined by the ratio of the mass source per unit depth to the viscosity,

$$\mathrm{Re} = \frac{S_0}{A_H H_0}, \tag{1.1}$$

and characterized the nonlinearity of the system. For low Reynolds number flow (i.e., $\mathrm{Re} < \mathrm{Re}_c \approx 30$), the potential vorticity was easily modified through a frictional boundary layer that spanned the full boundary current. In this regime, the circulation asymptotically approached a steady state. However, beyond a critical Reynolds number, the system exhibited a transition to time-dependent motion in which an eddy field appeared in the western boundary current. The authors showed that in this nonlinear regime, the turbulent boundary layer was essential to the potential vorticity transformation process, transferring vorticity from the inertial to frictional portions of the boundary current. The important dynamical contribution of the eddy field in that work leads to the question of its origin.

Of course, the tropical oceans commonly display significant variability in the vicinity of the western boundary current, both in nature and in other numerical models. As determined through current meter, satellite, surface drifter, and SOFAR float measurements, Johns et al. (1990) and Richardson et al. (1994) report substantial eddy generation in the upper-thousand meters of the tropical Atlantic Ocean. Deeper SOFAR float trajectories described by Richardson et al. (1993) reveal time-dependent trajectories extending down to 3300-m depth, and with current meters Johns et al. (1993) recorded fluctuations in the 4300-m core of the deep western boundary current at 8°N. Using a numerical model to study the tropical Indian Ocean, Cox (1979) described the development of eddies accompanying the sudden onset of monsoonal winds. Finally, in a study of the spinup of a cross-equatorial circulation, Kawase et al. (1992) found also in a three-dimensional ocean model the breakdown of the boundary current into a series of eddies propagating along the coast, even in the asymptotic limit of steady forcing.

The existence of these eddies and their dynamical role are now well established but their cause is not yet explained. The purpose of this paper is to analyze the instability of the tropical western boundary current and

Corresponding author address: Dr. Christopher A. Edwards, 3060 VLSB, Department of Integrative Biology, University of California, Berkeley, CA 94720-3140.

suggest a mechanism responsible for the eddy generation. Close examination of the eddy formation process in the numerical model applied by Edwards and Pedlosky (1998) reveals that the phenomenon is not only dependent on the Reynolds number of the flow but also on latitude. The eddies begin to develop for nonlinear flows with $\mathrm{Re} > \mathrm{Re}_c$, and (in the no-slip case) they form *preferentially* near the equator. This behavior is illustrated by the series of numerical experiments shown in Fig. 1. In all three cases, mass enters the basin in the northern end of the domain and leaves through a sink in the southern end. The basin has dimension, $L_x = 3$ and $L_y = 20$ (deformation radii), though the figures show only a fraction of this region to concentrate on the unforced portion near the western boundary and the equator. The system is accelerated from rest to a steady or quasi-steady state. In Fig. 1a, a western boundary current carries fluid laminarly from the source region across the equator to the sink region. Thus the flow is stable at this Reynolds number (Re = 25). In Fig. 1b, Re = 50 and the western boundary current is unstable, with eddies developing noticeably at the equator. Finally, Fig. 1c presents a run at Re = 50 that does not cross the equator. Its central latitude is at $y = 10$, and the flow is stable. It is the combination of a high Reynolds number and a constraint to cross the equator that stimulates the observed eddy field in these experiments.

While analysis of a midlatitude quasigeostrophic model by Ierley and Young (1991) has revealed that the Munk and more nonlinear boundary current profiles are unstable to infinitesimal perturbations, the latitudinal-dependence of this instability has not been discussed. In this paper, an idealized stability analysis of the inviscid shallow-water system reveals that the boundary current suffers a shear instability whose growth rate depends on the ratio of the zonal scale of the current to the internal deformation radius, which is maximum at the equator. The analysis is highly simplified. The beta effect is ignored. Only the role of the magnitude of the f as it determines the size of the deformation radius is considered. However, despite its shortcomings, the analysis predicts the properties of the instability as observed in the full numerical model with surprising accuracy and in a framework that is easily interpreted. The equatorially enhanced instability is responsible for the eddy field found in Edwards and Pedlosky (1998) which, in turn, expedites the cross-equatorial flow of the mean current. The addition of viscosity to the analysis merely damps the growth of the instability, suggesting that its inclusion is not essential to the eddy development except in its contribution to the structure of the mean field.

2. Formulation of the problem

The following presentation assumes standard notation, using Cartesian coordinates (x, y) in which the velocity field is given by (u, v), the depth of the shallow water layer by h, and subscripts denote partial derivatives. Assuming artificial body forces that maintain a purely meridional, latitude-independent basic state,

$$\overline{u} = 0; \qquad \overline{v} = \overline{v}(x); \qquad \overline{h} = \overline{h}(x), \tag{2.1}$$

the perturbation equations of the shallow-water system take the form

$$u'_t + \overline{v}\,u'_y - yv' + h'_x - A_H\nabla^2 u' = 0 \tag{2.2a}$$

$$v'_t + \overline{v}_x u' + \overline{v}\,v'_y + yu' + h'_y - A_H\nabla^2 v' = 0 \tag{2.2b}$$

$$h'_t + \overline{h}_x u' + \overline{v}\,h'_y + \overline{h}(u'_x + v'_y) = 0. \tag{2.2c}$$

Equations (2.2a–c) are in dimensionless form, with the prime variables representing variations from the basic state and overbars corresponding to the mean values. The coupled set of equations can be analytically simplified by making a stringent assumption. With the exception of the Coriolis parameter, y in this scaling, all of the coefficients of the dependent variables are functions of longitude only and not of latitude or time. *If* a local f-plane approximation is made and the Coriolis parameter is assumed to have a constant value, y_0, then a modal decomposition of the dependent variables is possible in y and t. Let

$$(v', h') = (V(x), H(x))e^{il(y-ct)} \tag{2.3a}$$

$$u' = ilU(x)e^{il(y-ct)}, \tag{2.3b}$$

where l is the meridional wavenumber of the disturbance and c represents its phase speed. The wavenumber-weighting of the zonal amplitude function in Eq. (2.3b) merely simplifies the ultimate form of the mathematical problem and represents no fundamental difference between the different components. The method outlined here is similar to that of Ni (1996) who considered a zonal flow in a multilayer, inviscid shallow-water model.

The f-plane approximation that allows this decomposition is a significant limitation of the present analysis as the variation of the Coriolis parameter is usually essential in tropical dynamical studies. A full treatment of the problem must include both the meridional variation of f and the downstream variation of the basic flow. However, it will be shown that this simple model provides surprisingly good agreement with numerical results, predicting the critical Reynolds number for onset of instability, the time and length scales associated with the perturbations, and the domain of their origin. In addition, it does so in a desirably simple and understandable framework that illustrates the essential dynamics of the breakdown of the boundary current. To be sure, there are equatorial modes that this model does not capture. However, these modes appear to be extraneous given the success of the simplified analysis to be presented. Furthermore, the numerical model results of Edwards and Pedlosky (1998) suggest that coupling to the equatorial waveguide begins at a higher Reynolds number than that at which the instability begins.

Using relations (2.3a) and (2.3b), the system (2.2a–c) reduces to

$$-l^2(\overline{v}-c)U - ilA_H(U_{xx}-l^2U) - y_0V + H_x = 0 \quad (2.4a)$$

$$(y_0+\overline{v}_x)U + (\overline{v}-c)V + \frac{i}{l}A_H(V_{xx}-l^2V) + H = 0 \quad (2.4b)$$

$$(\overline{h}_xU + \overline{h}U_x) + \overline{h}V + (\overline{v}-c)H = 0, \quad (2.4c)$$

where y_0 is the local value of y. Equations (2.4a–c) can be rewritten in the matrix form

$$\mathbf{A}\boldsymbol{\psi} = c\boldsymbol{\psi}, \quad (2.5)$$

where

$$\mathbf{A} = \begin{bmatrix} \overline{v} + ilA_H\left(\frac{1}{l^2}\frac{d^2}{dx^2} - 1\right) & \frac{y_0}{l^2} & -\frac{1}{l^2}\frac{d}{dx} \\ y_0 + \overline{v}_x & \overline{v} + ilA_H\left(\frac{1}{l^2}\frac{d^2}{dx^2} - 1\right) & 1 \\ \overline{h}_x + \overline{h}\frac{d}{dx} & \overline{h} & \overline{v} \end{bmatrix} \quad (2.6)$$

and

$$\boldsymbol{\psi} = \begin{bmatrix} U \\ V \\ H \end{bmatrix} \quad (2.7)$$

is the state vector. Solutions of the standard eigenvalue problem, (2.5) with nonzero imaginary components of the eigenvalue c signify growing and decaying modes.

To apply the stability analysis to a realistic shear flow of a western boundary current, Eq. (2.5) is solved in a channel whose finite zonal extent is large compared to the boundary-layer width. Boundary conditions at the solid meridional boundaries are no mass flux and no slip,

$$U = 0 \quad (2.8a)$$

$$V = 0. \quad (2.8b)$$

The scales of the basic states are identical to those of Edwards and Pedlosky (1998). Thus length scales are given in terms of deformation radii, growth rates are scaled by βL_D (with $L_D = \sqrt{c_0/\beta}$), and phase speeds are relative to the gravity wave speed $c = \sqrt{g'H}$. The nondimensional, undisturbed layer depth H_0 is unity in all cases examined here.

3. Inviscid shear instability

Although Eq. (2.5) can be discretized and analyzed as written for a variety of mean fields, it is of interest to examine the simpler, inviscid system first. Setting the viscosity coefficient A_H to zero eliminates viscous instability from the system. The matrix $\mathbf{A}$ then reduces to

$$\hat{\mathbf{A}} = \begin{bmatrix} \overline{v} & \frac{y_0}{l^2} & -\frac{1}{l^2}\frac{d}{dx} \\ y_0 + \overline{v}_x & \overline{v} & 1 \\ \overline{h}_x + \overline{h}\frac{d}{dx} & \overline{h} & \overline{v} \end{bmatrix}, \quad (3.1)$$

and the order of the system is reduced, so only Eq. (2.8a) is relevant. The new eigenvalue problem is defined by

$$\hat{\mathbf{A}}\psi = c\boldsymbol{\psi}. \quad (3.2)$$

The stability criterion for inviscid zonal flows on the β plane in the shallow-water system has been examined by Ripa (1983). The case with $\beta = 0$ corresponds to the present system. Stability is insured if (i)

$$[\alpha - \overline{v}(x)]\frac{d\overline{q}}{dx} \geq 0, \quad (3.3)$$

and (ii)

$$[\alpha - \overline{v}(x)]^2 \leq \overline{h}(x) \quad (3.4)$$

for all x and any α. The potential vorticity is defined as

$$\overline{q} = \frac{y_0 + \overline{v}_x}{\overline{h}}. \quad (3.5)$$

For the standard Munk boundary current as well as inertio–viscous profiles, condition (3.3) is generally violated assuming α in the range of the velocity.

Eigenvalue equation (3.2) is discretized on a stretched grid in x with staggered variables. For this application, the stretching function is a simple exponential:

$$x(i) = d(e^{sn/N} - 1), \quad (3.6)$$

where

$$d = \frac{x_E}{e^s - 1}, \quad (3.7)$$

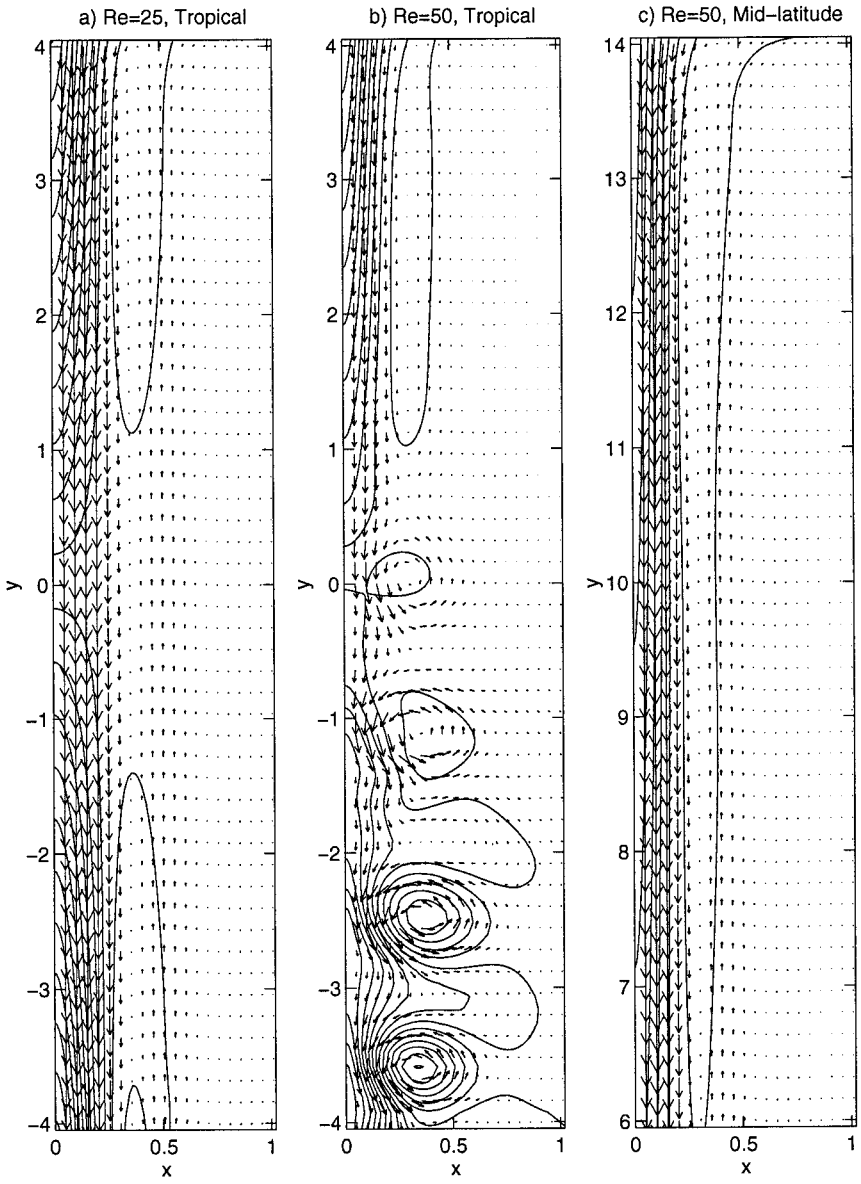

FIG. 1. Velocity and height fields in a subdomain of the basin with source in the north and sink in the south at $t = 1000$: (a) Re = 25 and central latitude is the equator; (b) as in (a) but with Re = 50; (c) as in (b) but with central latitude at $y = 10$.

N is the number of grid points, and s gives the degree of stretching. A value of $s = 3$ was chosen to adequately enhance the resolution in the rapidly varying western boundary region without introducing excessive deformation of the grid. All calculations were determined using a value of at least $N = 100$, though even $N = 32$ appears adequate to reveal the general behavior of the instability. The channel width is 20 Munk boundary layer widths or more. Eigenvalues, c, and eigenvectors, $\boldsymbol{\psi}$, are determined using the eigenvalue solver, eig.m, which calls industry standard EISPACK routines and is included in the basic distribution of Matlab. Checking the solutions using a different solver, sptarn.m, which applies a different algorithm to find selected eigenvalues produces virtually indistinguishable results. The numerical method for solution was checked against and agreed well with the asymptotic stability analysis of Lipps (1963) for a wall-free Bickley jet.

4. Instability of the Munk boundary layer

We begin with a simple basic state in which the fields are truly latitude independent. Thus any asymmetry that develops in the instability characteristics can then be attributed to the shallow-water system and not to the meridional variation in the potential vorticity structure

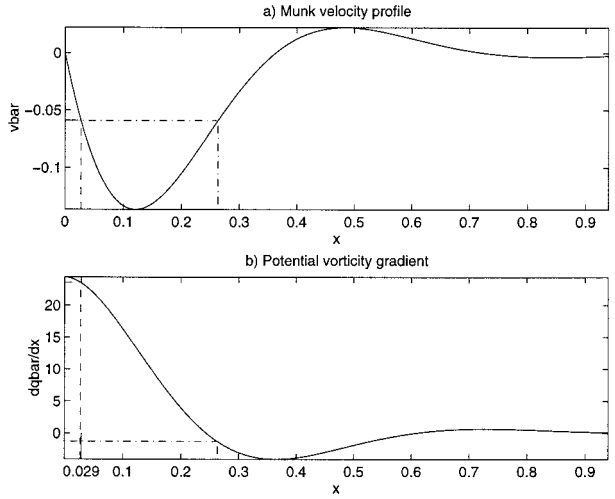

FIG. 2. (a) Velocity and (b) potential vorticity gradient for the Munk boundary layer with $\delta_M = 0.1$ and $S_0 = 0.025$. Only shown to $x = 1$, though $x_E = 2$ in calculations below. Dot-dashed curve marks the intersection, $\overline{v} = 0.059$, which equals the phase speed of the fastest unstable mode with $l = 6$.

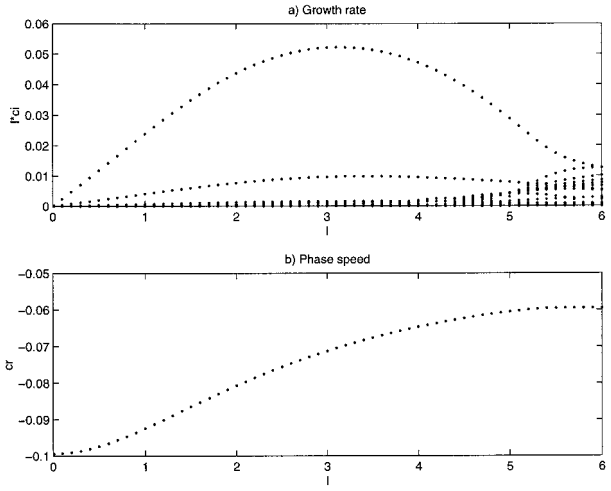

FIG. 3. (a) Growth rates as a function of meridional wavenumber for the velocity profile in Fig. 2 in the inviscid shallow-water system. Decaying modes (not shown) are complex conjugate solutions. (b) Phase speeds for the fastest growing modes in (a).

of the basic state. It can be shown that using a more realistic, latitude-dependent flow field determined by the numerical model produces very similar results.

The analytic solution to the Munk boundary layer provides a convenient basic velocity profile:

$$\overline{v}(x) = D \sin\left(\frac{\sqrt{3}\,x}{2\delta_M}\right) e^{-(x/2\delta_M)}, \tag{4.1}$$

where

$$D = -\frac{2S_0}{\sqrt{3}\,\delta_M}. \tag{4.2}$$

Rather than use the geostrophically balanced height field, which varies with latitude, we set the height of the layer uniform:

$$\overline{h} = 1. \tag{4.3}$$

The Munk layer is determined using $\delta_M = (A_H/\beta)^{1/3} = 0.1$ and for a boundary layer transport of $S_0 = 0.025$, consistent with the numerical model runs in Fig. 1. Equation (3.2) is solved for the profile, Eq. (4.1), and a Coriolis parameter, $y_0 = 1$. The basic-state velocity profile is shown in Fig. 2 along with the zonal gradient of the potential vorticity. The potential vorticity gradient passes through zero at multiple longitudes so the inflection point criterion is satisfied by this basic state.

The growth rates, $\mathrm{Im}(lc) = \omega_i$, of all nondecaying eigenmodes of the system are shown in Fig. 3a as a function of the wavenumber l. The number of modes equals the dimension, $3N$, of the system. Most modes are neutral, with zero imaginary component, and all modes are complex conjugates though only growing modes are shown. Equation (3.2) has complex conjugate solutions because $\hat{\mathbf{A}}$ defined by Eq. (3.1) is real.

In Fig. 3a a few sets of unstable modes can be traced as a function of wavenumber. In particular, one set of modes has the largest amplitude for all l, and its maximum occurs at a value of approximately $l = 3.25$. This set and the additional sets of modes that appear within its envelope are quite insensitive to the discretization and grid resolution. At high wavenumber there exist an increasing number of unstable modes of small amplitude. These are more fragile modes that depend more closely on the discretization of the system. While all unstable modes grow, it is the one with the largest growth rate that dominates the instability. Therefore these numerically sensitive modes can be neglected when considering also those more unstable. Within the approximations of the analysis, Fig. 3a indicates that the Munk layer is unstable to inviscid, growing perturbations.

The phase speed of the fastest growing mode is shown as a function of wavenumber in Fig. 3b. The value varies between $c_r = -0.098$ at $l = 0.01$ and $c_r = -.059$ at $l = 6$, both in the range of $\overline{v}$ and consistent with Howard's semicircle theorem.

The amplitudes of the eigenvectors (e.g., $\sqrt{UU^*}$) associated with the fastest growing modes are shown in Fig. 4. The zonal velocity and height fields are smooth functions of longitude, with a noticeable maximum between $x = 0.3$ and $x = 0.5$, depending on the wavenumber. At high wavenumbers, the eigenfunctions show the rise of a second peak near $x = 0.1$. The V component also has an interesting two peak structure, with a third, particularly sharp, feature developing for high wavenumbers. The eigenfunctions are very smooth for long-wave solutions. The sharpest peak at high wavenumber is associated with the critical location where the Munk velocity profile equals the phase speed of the fastest growing mode,

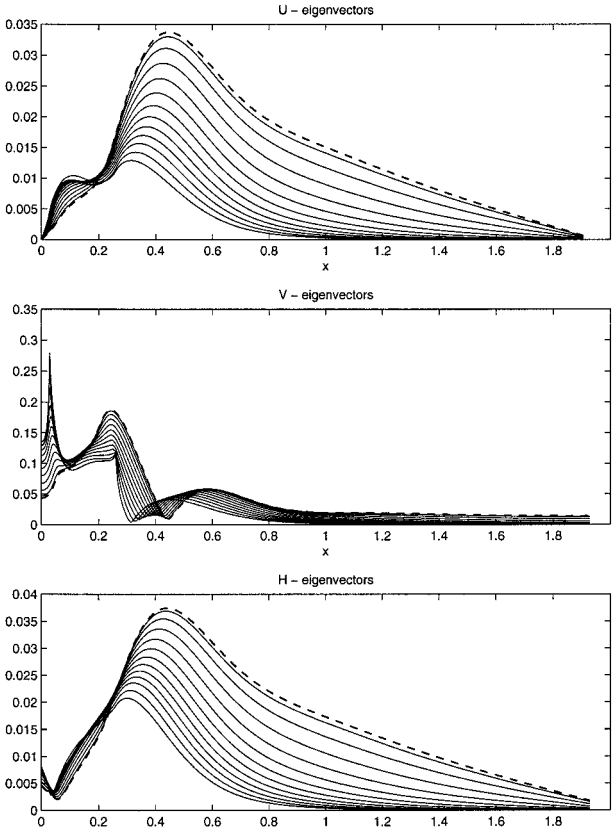

FIG. 4. Eigenfunction amplitudes of the most unstable modes in Fig. 3 at intervals of $l = 0.5$: (a) U, (b) V, and (c) H. The dashed curve corresponds to $l = 0.01$.

$$\overline{v}(x) = c_r^1. \tag{4.4}$$

For a jet profile with the phase speed in the range of the velocity field, this relation is satisfied at least at two longitudes. From Fig. 3 it is clear that $\overline{v} = 0.059$ corresponds to the phase speed of the fastest growing mode at $l = 6$. This line is overlayed as a dot-dashed curve in Fig. 2a. Equality (4.4) applies at the intersection of the two curves. The first intersection occurs at $x = 0.275$, which corresponds closely to the peak in the eigenvector amplitude at $x = 0.029$. The second intersection occurs at $x = 0.262$, where the potential vorticity gradient $d\overline{q}/dx$ is nearly zero. Thus the asymmetry of the Munk boundary layer appears to play a role in the development of the strong peak in the eigenvector curve. It occurs approximately at the location determined by Eq. (4.4) but the one that does not satisfy.

$$\frac{d\overline{q}}{dx} \approx 0. \tag{4.5}$$

Identical analyses for a range of latitudes provide the growth rate as a function of wavenumber and latitude, y_0. This field is contoured in Fig. 5a for the same Munk layer used above. Solid lines separate intervals of a hundredth and two dot-dashed contours at values of

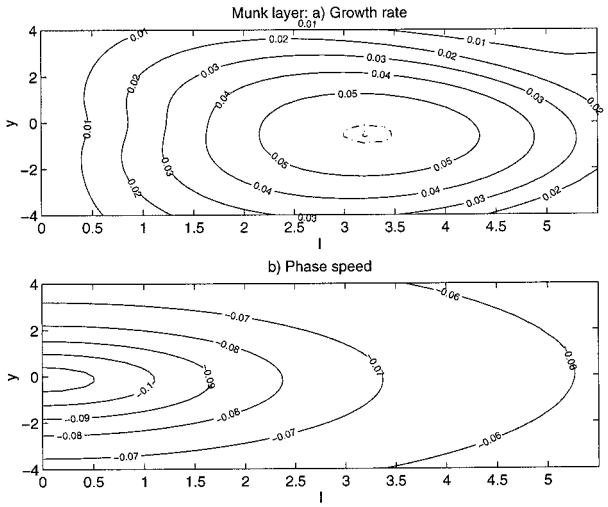

FIG. 5. As functions of meridional wavenumber and latitude, the (a) growth rate and (b) phase speed of the fastest growing mode for the Munk boundary layer in Fig. 2. The dot-dashed curves in (a) mark $\omega_i = 0.058$ and 0.0584.

$\omega_i = 0.058$ and 0.0584 are used to aid the eye. A growth rate maximum $[\omega_i]_{\max} = 0.0584$ resides clearly in the immediate vicinity of the equator, at a wavenumber $l = 3.2$ and at a latitude of $y_0 = -0.5$. Note that this growth rate maximum is not located at $y_0 = 0$. Since the basic state is independent of y, it appears that the shallow-water system is aware of the direction of the flow through the absolute vorticity, $y_0 + \overline{v}_x$, in matrix $\hat{\mathbf{A}}$.

The phase speed of the fastest growing mode is contoured in Fig. 5b also as a function of wavenumber and latitude. For a given wavenumber, the phase speed of the most unstable disturbance decreases with latitude.

5. Geostrophic perturbations

Although it is clear that the Munk boundary current is unstable to inviscid perturbations, the reason for the tropical enhancement is not clear from the form of matrix $\hat{\mathbf{A}}$. To interpret this behavior, a simpler system is studied. Following the examples of Stern (1961) and Lipps (1963), and in dimensional form using $f = \beta y_0$, the mean flow is assumed only weakly nonlinear so that

$$\overline{v}_x \ll f, \tag{5.1}$$

and the perturbations must be geostrophically balanced:

$$-fv' = -g'h'_x \tag{5.2a}$$

$$fu' = -g'h'_y. \tag{5.2b}$$

Clearly these approximations are invalid very close to the equator, but the flow can be specified to be arbitrarily weak, leading to reliable calculations at latitudes arbitrarily close to $y = 0$.

The geostrophic approximation couples the different fields of the disturbance such that a single equation results, expressed in terms of a single variable. Adopting

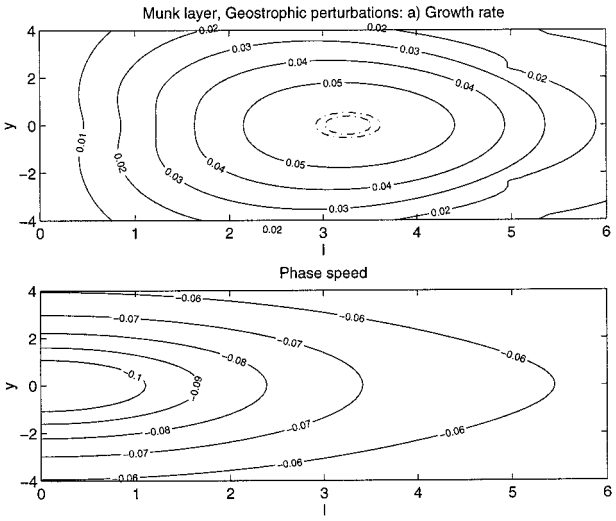

FIG. 6. As functions of meridional wavenumber and latitude, the (a) growth rate, and (b) phase speed for the fastest growing mode as in Fig. 5 but assuming geostrophic perturbations as in Eq. (5.3).

the above approximations and scaling the horizontal dimensions by the length scale L yields for the height anomaly H,

$$(\overline{v} - c)[H_{xx} - (l^2 + F)H] - (\overline{v}_{xx} - F\overline{v})H = 0, \quad (5.3)$$

where

$$F \equiv \frac{L^2 f^2}{g'\overline{h}} \quad (5.4a)$$

$$= \left(\frac{L}{L_D}\right)^2 \quad (5.4b)$$

is the rotational Froude number. At the boundaries, the height of the disturbance is set to zero:

$$H = 0. \quad (5.5)$$

Equation (5.3) describes the *initial* development of the instability for weak mean flows until the Rossby number of the disturbance lU'/f, becomes order 1. For $F = 0$, Eq. (5.3) reduces to the familiar Rayleigh equation or the equation for standard barotropic instability. The additional terms proportional to F reflect the influence of the horizontal divergence in the velocity field that is included in the shallow water model.

The solution to Eq. (5.3) subject to boundary conditions in Eq. (5.5) gives remarkably similar results to that of the full system. The contour plot of growth rate as a function of wavenumber and latitude is shown in Fig. 6a using the same basic state. Solid contours are uniform, every hundredth, and the dot-dashed contours correspond to values $\omega_i = 0.058$ and 0.0584 as in Fig. 5a. The maximum of 0.0588 is located at a wavenumber of $l = 3.26$ and $y = 0$. Note that there is no asymmetry in this modified instability problem as Eq. (5.3) cannot distinguish between the Northern and Southern Hemispheres if the basic state is latitude independent.

The close similarity between Figs. 6 and 5 suggests that the physics of the tropical enhancement is essentially quasigeostrophic, appearing even in the presence of perturbations constrained to a geostrophic balance. One interpretation follows from the perspective of energetics. In the context of this simplified treatment, it is possible to derive the energy equation,

$$\int_0^{x_E} dx \frac{\partial}{\partial t}\left[\frac{1}{2}\left(\overline{(H_x)^2}^y + \overline{(H_y)^2}^y\right) + \frac{1}{2}F\overline{H^2}^y\right] = \int_0^{x_E} dx\, \overline{H_x H_y}^y \overline{v}_x. \quad (5.6)$$

Here, the overbar symbol with a y superscript implies an averaging in the y direction. Zonally integrated, the time evolution of total energy of the disturbance depends on the ability of the disturbance to extract energy from the mean flow through the Reynolds stress, $\overline{H_x H_y}^y$.

The total energy is divided between potential, the last term on the left-hand side of Eq. (5.6), and kinetic, the first two terms, and their ratio is $O(F)$. At midlatitudes, F is large, and most of the energy of the disturbance is partitioned into potential form (P). In contrast, near the equator the fraction of total energy that is kinetic (K) reaches its maximum. However, from the right-hand side of Eq. (5.6), it is clear that the growth of the instability is proportional to the Reynolds stress, and the Schwarz inequality allows

$$(H_x H_y) \le \frac{(H_x)^2 + (H_y)^2}{2}. \quad (5.7)$$

For solutions of the form

$$H = \hat{H}(x)\cos[l(y - c_r t)]e^{\sigma t}, \quad (5.8)$$

it can be shown that

$$\int dx\, \sigma(K + P) \le \int dx\, K(\overline{v}_x)_{\max}, \quad (5.9)$$

or

$$\sigma \le (\overline{v}_x)_{\max} \frac{\int dx\, K}{\int dx\, (K + P)}. \quad (5.10)$$

Thus the growth rate of the disturbance is bounded by the ratio of the kinetic energy to the total energy. When the partitioning favors potential energy, this ratio is small, and the growth rate is bounded by a smaller value than when more of the energy is in kinetic form. Not intended as a rigorous proof, this description nonetheless suggests that at the equator, where the system is most barotropic and the kinetic energy dominates, the disturbance extracts energy from the mean flow most

efficiently. In contrast, at midlatitudes, much of the energy is stored in layer height variations. As a result, Reynolds stress is more strongly bounded, and the accompanying instability is more subdued. It follows from Eq. (5.3) that the stability boundary of the flow and, in particular c_i, can only be a function of the square of the total wavenumber $l^2 + F$. However, the growth rate σ is lc_i, so the maximum rate of growth for any mode of instability will occcur when $F = 0$, or in our parametric model, at the equator.

It is important to note that the original work of Lipps (1963) illustrated the stabilizing effect of divergence on a zonal midlatitude flow, and this work was extended to the equator by Philander (1976).

6. The influence of viscosity

As viscosity is an essential part of the dynamics of the mean flow, it can be expected to influence the dynamics of the perturbation. Indeed, that the system is stable for some Reynolds numbers shows that its effect is not negligible. The eigenvalue problem including dissipation along with the extra, no-slip boundary condition is solved similarly to the above inviscid calculations. This section describes the stability of two basic states both taken from the full shallow-water numerical model results under different parameter settings. Their stability is examined for a range of viscosities applied to the perturbations. The first basic state is shown in Fig. 1a, and it has a Munk boundary layer width of $\delta_M = 0.1$ and a source strength of $S_0 = 0.025$. The second is identical except that $\delta_M = 0.05$ and $S_0 = 0.003$.

Numerical results, not shown, for the first mean state indicate that this flow is unstable for a range of Reynolds numbers. Unlike in the inviscid calculations, the eigenmodes are no longer conjugate pairs, but one set of modes clearly shows growing perturbations over a window of wavenumbers. Another change from the previous calculations is a shift in the wavenumber of maximum growth rate, from near $l = 3.25$ in the inviscid case to approximately $l = 4$ with viscous perturbations.

The amplitudes of the eigenfunctions of the unstable modes determined using a viscosity, $A_H = 2.5 \times 10^{-4}$ (Re = 100), are shown in Fig. 7. Their similarity to the inviscid case is striking, even using a slightly different basic state. One distinguishing feature of the viscous modes is found in the amplitudes of the V eigenfunctions. As in the previous example, a peak appears at small x in the functions corresponding to large wavenumber. However, the peak is broader than in the inviscid case suggesting that viscosity plays an important role in the dynamics of the critical layer.

Calculations at several latitudes show similar bullseye patterns of growth enhanced near the equator but with reduced amplitude depending on the magnitude of the viscosity employed. For example, using a viscosity of 8.333×10^{-4}, which corresponds to Re = 30, gives a maximum growth rate, $[\omega_i]_{\max} = 0.014$, centered at $l = 3.8$ and $y = -1.2$. Increasing the dissipation appears to drive the instability further south of the equator and lengthen the time needed for its development. The shift to a higher wavenumber is found consistently at all latitudes.

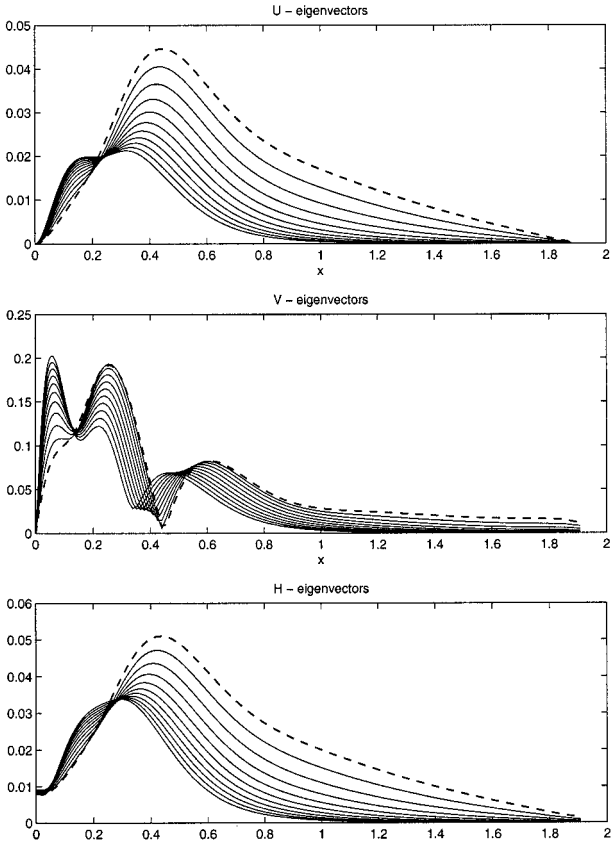

FIG. 7. Eigenfunction amplitudes of a subset, $l = 1$ to $l = 6$ in intervals of 0.5, of the fastest growing modes obtained using the basic state in Fig. 1a and Re = 100 for the perturbation: (a) U, (b) V, and (c) H. Notice the broad peak in the V eigenfunction near $x = 0.05$. The dashed curve corresponds to $l = 1$.

This highly idealized viscous theory indicates that the numerical model should be unstable for Re = 25. In fact, numerical integrations indicate that the instability begins near Re = 32. This small discrepancy may result from the approximations of the instability calculation itself (e.g., neglect of the variation in f). Also, the numerical model may in fact be unstable for Re = 25. The timescale for growth of the instability at this Reynolds number is $O(5000)$ time units, a very long integration that has not been examined. At Re = 32 the timescale is $O(300)$ time units, which is the timescale over which they are observed to develop. Thus the numerical model may be unstable at smaller Reynolds numbers than Re = 32 but so slightly that the time-dependent motion escapes detection.

A second measure of the accuracy of the instability calculation is to compare the length scales of the disturbance predicted by the theory to that found in the

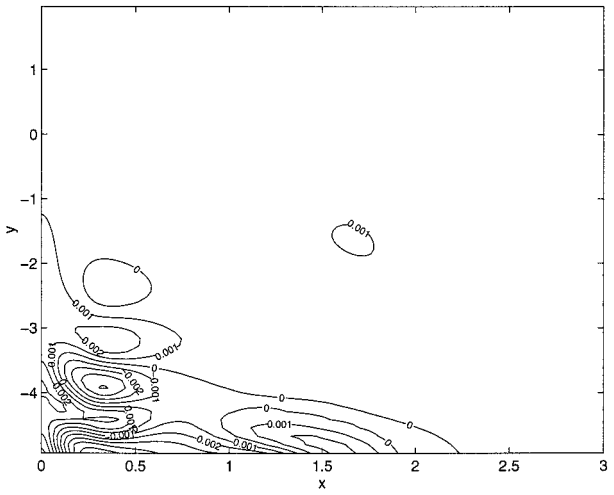

FIG. 8. The height field anomaly after instability begins. The difference in height fields between steady solution at Re = 31.25 to Re = 32.25 after 300 time units.

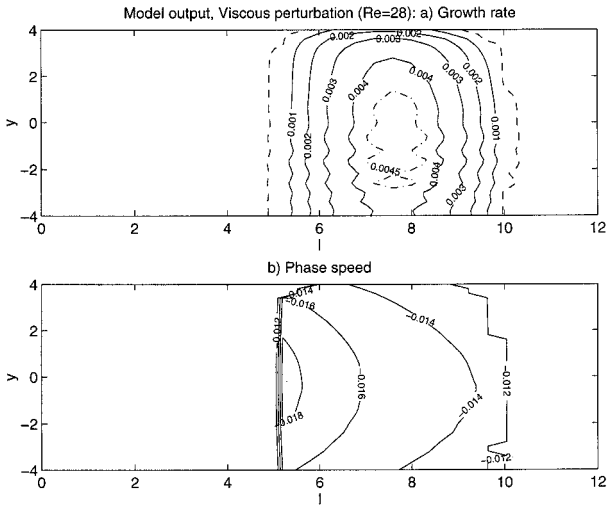

FIG. 9. As functions of meridional wavenumber and latitude, (a) growth rates and (b) phase speeds of the most unstable modes for the basic state (not shown) with $\delta_M = 0.05$, using a viscosity of $A_H = 1.071 \times 10^{-4}$ (Re = 28 for the perturbations). The dashed contour corresponds to a value of $\omega_i = 10^{-4}$ and divides the domain into regions of growth and regions of stability.

numerical experiment. After reaching an approximate steady state at Re = 31.25, the viscosity of the numerical model was changed slightly to Re = 32.25, and integrated further in time. Figure 8 presents the difference in the height fields after 300 time units have elapsed. Height anomalies appear just south of the equator as expected from the theory and develop farther to the south. There is some variability being swept eastward from the western boundary near the southern boundary of the plot, where the boundary current veers eastward as part of the Southern Hemisphere sink. Approximately one full wave is visible in the figure, and it has a wavelength of approximately 1.5 deformation radii. This wavelength agrees well with that predicted by the theory: if $l = 3.8$, $\lambda = 1.65$. Thus even with the extensive idealizations of the theory, it predicts the behavior of the disturbances found in this numerical model, in location for growth, in wavelength, and in the critical Reynolds number.

The numerical example described above contains eddies that are approximately of the deformation scale, consistent with the linear theory and the basic state applied. To show that these results are not coincidental and thus further support the relevance of the highly idealized analysis to the full numerical model results we examine a second numerical experiment in which the viscosity has been reduced by a factor of 8. Setting $A_H = 1.25 \times 10^{-4}$, a steady solution results from using $H = 1$ and $S_0 = 0.003$. For these parameters, Re = 24 is just below the critical value at which time-dependent motion begins, which indicates that Re_c is not a universal number but varies with model parameters, such as δ_M/L_D.

The growth rates and phase speeds for this experiment using $A_H = 1.071 \times 10^{-4}$ (Re = 28) are shown in Fig. 9 as functions of meridional wavenumber and latitude. Note that the growth rate maximum occurs at a meridional wavenumber of $l = 7.6$, approximately twice the value in the former experiment and consistent with the smaller boundary current of this experiment. The bullseye for this run is also somewhat more extended meridionally from the previous examples, showing that as the boundary current narrows with respect to the deformation radius and the system becomes more barotropic, the tropical enhancement to the instability is less pronounced.

To compare the growth rates predicted by the theory to those observed in the model, we further integrate this numerical experiment at the lower viscosity ($A_H = 1.071 \times 10^{-4}$). This exercise generates cyclonic structures in the vicinity and south of the equator much as in Fig. 1b but of a smaller scale. Showing the zonal velocity anomaly, $du = u(t_0 + \Delta t) - u(t_0)$ at intervals of $\Delta t = 400$, Fig. 10 presents the time evolution of the instability. The contour interval is the same in each plot ($du = 0.002c$). After the first time interval, the western boundary current has superposed on it a series of very weak structures of alternating sign. After $\Delta t = 800$ well-defined eddies of alternating sign emerge between $y = -1$ and $y = -5$. As time continues, the variability grows in strength and in meridional extent. After 1600 time units, the eddies exist north of the equator, and the strength of those near $y = -3$ have peaked in strength.

Although the negative anomalies (dashed in the figure) tend to be slightly larger in magnitude than the positive, there is very good symmetry between positive and negative features. This remains true for the meridional velocity and height fields as well, though the vorticity field shows a more pronounced asymmetry favoring positive anomalies. This symmetry supports the present analysis as the anomalies are consistent with the

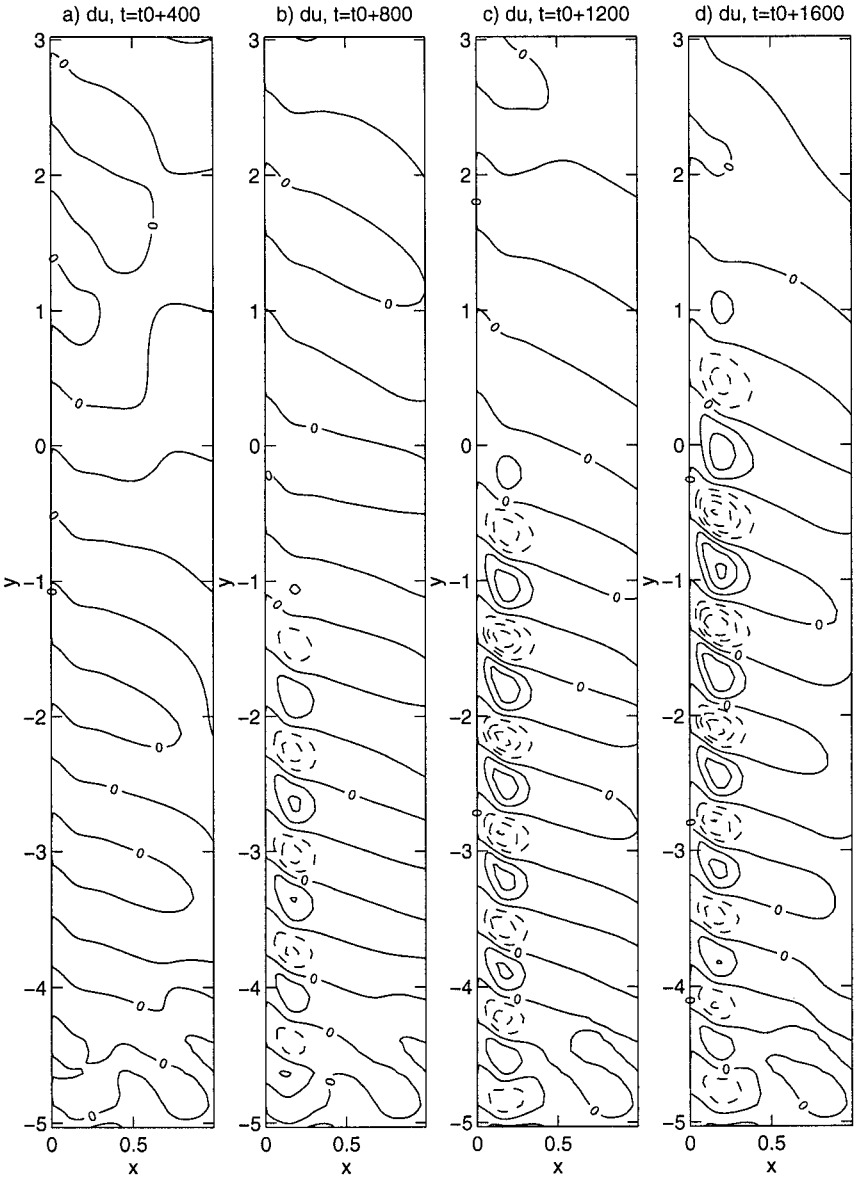

FIG. 10. Zonal velocity anomalies for the basic state described in Fig. 9 at intervals of Δt = 400 showing the development of the eddy field after the time t_0 = 1000 when the Reynolds number of the system was adjusted from 24 to 28.

modal decomposition of the u, v, and h fields in Eqs. (2.3a) and (2.3b). The timescale for the eddy development in the model is 800 to 1000 time units, slightly less than the value predicted by the viscous theory of 1300 but somewhat longer than that predicted by the inviscid calculation (roughly 250). The fully developed anomalies in Fig. 10d have a characteristic wavelength of between 2/3 and 1 deformation radius, depending on the latitude at which the estimate is made. The value predicted by the stability analysis is $\lambda = 2\pi/7.6 \approx 0.8$. The purely inviscid calculation predicts a wavelength of approximately 1 deformation radius. The simple, highly idealized theory predicts reasonably 1) the time and space scales of the eddies, 2) their location for development, 3) their structure, and 4) the critical Reynolds number at which they appear.

The addition of viscosity to the system has adjusted the instability properties slightly, shifting the wavenumber at which the maximum growth rate is found and reducing the amplitude of the growth. However, it has not produced a qualitative change in the development of the system. Viscosity acts as a stabilizing influence, but the physics of the instability remains unaltered. These features suggest that the instability mechanism

responsible for the growth of the eddies in the time-dependent model is classical shear instability and not viscous instability.

7. Summary

A linear stability analysis of parallel flow in a shallow-water model using a local f-plane approximation indicates that the western boundary current is unstable to infinitesimal perturbations and that this instability is greatest in the vicinity of the equator. The simplified calculations successfully predict the time and length scales for the growth of the instability, the critical Reynolds number at which time-dependent motion appears, and its tendency to form near the equator, as found in a β-plane numerical model.

Close similarities in properties of growing modes between the shallow-water and a more restrictive quasigeostrophic model suggest that the latitudinal dependence of the instability reflects the meridional variation of the internal deformation radius. At the equator where the deformation radius is a maximum, the system is most barotropic, and the Reynolds stress is most efficient at extracting energy from the mean flow to drive the perturbations. This behavior is well known in quasigeostrophic zonal flows (e.g., Lipps 1963; Philander 1976), but its relevance to meridional flows on a β plane is not obvious a priori. Indeed, the agreement between the simplified analysis and the numerical results is somewhat remarkable, given the strong variation of the planetary vorticity in the region.

The instability of the western boundary current has previously been investigated at midlatitudes by Ierley and Young (1991) and Cessi and Ierley (1993). These studies conclude that viscosity plays a fundamental role in generating the eddy field. In contrast, we find that the growth rate is maximum in the limit in which the perturbation dynamics are inviscid. The addition of viscosity to the analysis offers no significant qualitative difference in the eigenfunctions that describe the growing modes. As viscosity does not appear to be necessary to transfer energy from the mean field to the perturbation, we argue instead that the instability does not result from or depend primarily on viscous processes, but is basically an inviscid shear instability.

One important implication of this conclusion is that the generation of the eddy fields found in tropical models is inevitable for sufficiently nonlinear flow. Given sufficient resolution of the boundary current, such models should produce eddy fields consistent with those found in nature, regardless of the dissipative parameterization, provided that it produces a physically realistic western boundary current profile with an inflection point in its profile. Thus the dynamical role attributed to the eddies in Edwards and Pedlosky (1998) represents a robust aspect of the nonlinear shallow-water system and is not critically dependent on the choice of dissipation applied.

Acknowledgments. This research, which contributed to CAE's Ph.D. thesis, was supported in part by the National Science Foundation under Grant OCE-9115915 and by the Office of Naval Research through Grant N00014-94-1-0844. Many helpful discussions with Drs. John Marshall, Glenn Flierl, Mike Spall, Bruce Warren, and Nelson Hogg greatly improved this work.

REFERENCES

Cessi, P., and G. R. Ierley, 1993: Nonlinear disturbances of western boundary currents. *J. Phys. Oceanogr.,* **23,** 1727–1735.

Cox, M. D., 1979: A numerical study of Somali Current eddies. *J. Phys. Oceanogr.,* **9,** 311–326.

Edwards, C. A., and J. Pedlosky, 1998: Dynamics of nonlinear cross-equatorial flow. Part I: Potential vorticity transformation. *J. Phys. Oceanogr.,* **28,** 2382–2406.

Ierley, G. R., and W. R. Young, 1991: Viscous instabilities in the western boundary layer. *J. Phys. Oceanogr.,* **21,** 1323–1332.

Johns, W. E., T. N. Lee, F. Schott, R. J. Zantopp, and R. H. Evans, 1990: The North Brazil Current retroflection: Seasonal structure and eddy variability. *J. Geophys. Res.,* **95,** 22 103–22 120.

——, D. M. Fratantoni, and R. J. Zantopp, 1993: Deep western boundary current variability off northeastern Brazil. *Deep-Sea Res.,* **40,** 293–310.

Kawase, M., L. M. Rothstein, and S. R. Springer, 1992: Encounter of the deep western boundary current with the equator: A numerical spin-up experiment. *J. Geophys. Res.,* **97,** 5447–5463.

Lipps, F. B., 1963: Stability of jets in a divergent barotropic fluid. *J. Atmos. Sci.,* **20,** 120–129.

Ni, B., 1996: Temporal, spatial and pulse instabilities of the gulf stream. Ph.D. thesis, Massachusetts Institute of Technology and Woods Hole Oceanographic Institute Joint Program in Oceanography, 206 pp.

Philander, S. G. H., 1976: Instabilities of zonal equatorial currents. *J. Geophys. Res.,* **81,** 3725–3735.

Richardson, P. L., and W. J. Schmitz Jr., 1993: Deep cross-equatorial flow in the Atlantic measured with SOFAR floats. *J. Geophys. Res.,* **98,** 8371–8387.

——, G. E. Hufford, R. Limeburner, and W. S. Brown, 1994: North Brazil Current retroflection eddies. *J. Geophys. Res.,* **99,** 5081–5093.

Ripa, P., 1983: General stability conditions for zonal flows in a one-layer model on the β-plane or the sphere. *J. Fluid Mech.,* **126,** 463–489.

Stern, M., 1961: The stability of thermoclinic jets. *Tellus,* **13,** 503–508.